Textile-Type Lithium-Ion Battery Cathode Enabling High Specific/Areal Capacities and High Rate Capability through Ligand Replacement Reaction-Mediated Assembly

Minseong Kwon, Donghyeon Nam, Seokmin Lee, Yongju Kim, Bongjun Yeom, Jun Hyuk Moon, Seung Woo Lee,* Yongmin Ko,* and Jinhan Cho*

Achieving high energy storage performance and fast rate capability at the same time is one of the most critical challenges in battery technology. Here, a high-performance textile cathode with notable specific/areal capacities and high rate capability through an interfacial interaction-mediated assembly that can directly bridge all interfaces existing between textile and conductive materials and between conductive and active materials, minimizing unnecessary insulating organics is reported. First, amine (NH_2)- and carboxylic acid (COOH)-functionalized multiwalled carbon nanotubes (MWNTs) are alternately layer-by-layer (LbL)-assembled onto cellulose textiles for the preparation of conductive textiles using hydrogen bonding interactions. Dioleamide-stabilized $LiFePO_4$ nanoparticles (DA-LFP NPs) with high crystallinity and high dispersion stability in organic media are consecutively LbL-assembled with $MWNT-NH_2$ onto conductive textiles through ligand replacement between native DA ligands bound to the surface of the LFP NPs and NH_2 groups of MWNTs. In this case, 35 nm sized LFP NPs are densely and uniformly adsorbed onto all regions of the textile, and additionally, their areal capacities are increased according to the deposition number without a significant loss of charge transfer kinetics. The formed textile cathodes exhibit remarkable specific/areal capacities (196 mAh g^{-1}/8.3 mAh cm^{-2} at 0.1 C) and high rate capability with highly flexible mechanical properties.

1. Introduction

Enormous interest and explosive growth for the use of variable portable/soft electronic devices have strongly increased the demand for rechargeable batteries with higher energy density, fast rate capability, and long-term stability. In particular, the mechanical flexibility of batteries for soft electronics should be well adapted to various motions and shapes of the human body beyond simply putting and carrying them on the body. Therefore, for the preparation of high-performance batteries that can satisfy the abovementioned electrochemical and mechanical properties at the same time, it is critical to develop high-quality electrode components (i.e., energy materials and flexible conductors) and to design an optimal electrode structure that can maximize their functionalities.

Most flexible lithium-ion batteries (LIBs) are manufactured by slurry casting powder-type active materials and additives (i.e., active energy materials, insulating polymer binders, and conductive carbon materials) on nonporous metal foils, which imposes a limit on realizing higher energy density and mechanical resilience.[1,2] That is, increasing the mass loading of the randomly mixed active slurry on nonporous substrates inevitably causes an increase in internal resistance due to the thickened film thickness (typically up to several hundred micrometers thick[3]), resulting in the loss of energy storage efficiency and rate capability.[4,5] In

M. Kwon, D. Nam, S. Lee, Prof. J. Cho
Department of Chemical and Biological Engineering
Korea University
145 Anam-ro, Seongbuk-gu, Seoul 02841, Republic of Korea
E-mail: jinhan71@korea.ac.kr
Prof. Y. Kim, Prof. J. Cho
KU-KIST Graduate School of Converging Science and Technology
Korea University
145 Anam-ro, Seongbuk-gu, Seoul 02841, Republic of Korea
Prof. B. Yeom
Department of Chemical Engineering
Hanyang University
222 Wangsimni-ro, Seongdong-gu, Seoul 04763, Republic of Korea

The ORCID identification number(s) for the author(s) of this article can be found under https://doi.org/10.1002/aenm.202101631.

Prof. J. H. Moon
Department of Chemical and Biomolecular Engineering
Sogang University
Baekbeom-ro 35, Mapo-gu, Seoul 04107, Republic of Korea
Prof. S. W. Lee
The George W. Woodruff School of Mechanical Engineering
Georgia Institute of Technology
Atlanta, GA 30332, USA
E-mail: seung.lee@me.gatech.edu
Dr. Y. Ko
Division of Energy Technology
Daegu Gyeongbuk Institute of Science and Technology (DGIST)
333 Techno Jungang-daero, Hyeonpung-eup, Dalseong-gun,
Daegu 42988, Republic of Korea
E-mail: yongmin.ko@dgist.ac.kr

ADVANCED
SCIENCE NEWS
www.advancedsciencenews.com

ADVANCED
ENERGY
MATERIALS
www.advenergymat.de

particular, the unfavorable interfacial interactions and quite different tensile properties between the bulky active composite and the substrate lead to serious structural failures under successive mechanical deformations.[4]

Recently, conductive textile-based electrodes have emerged as promising candidates for resolving the drawbacks of nonporous substrate-based electrodes and enhancing the energy and power performance of LIBs, and various approaches have been also conducted for their performance analysis.[6–9] The unique 3D porous structure of a conductive textile (i.e., a current collector) consisting of numerous interconnected fibrils not only provides an extremely large specific surface area for the mass loading of energy material in the unit area but also facilitates ion diffusion into active materials (i.e., good electrolyte wettability), allowing superior electrochemical performance over nonporous electrodes.[2,10–12]

To maximize the advantages of these textile substrates, solution-processable conductive materials such as carbon nanotubes (CNTs), reduced graphene oxides, and/or conducting polymers have been incorporated into various textiles,[13–18] and furthermore, high-energy materials (e.g., transition metal oxide particles) have been blended with conductive additives to supplement their poor electrical conductivity. However, these approaches have the fundamental limitation of depositing energy materials uniformly and densely onto all regions of conductive textiles.[19] Specifically, the conventional slurry casting method cannot minutely control the interfacial interactions between active materials and conductive textile, which significantly limits the mechanical stability and electrical transfer at the interface. Therefore, it is highly desirable to develop new deposition processes that can control the interfacial interactions between neighboring active materials and conductive additives and conductive textiles and active materials.

The specific capacity of cathode materials is much lower than that of anode materials (e.g., graphite or Si), which has restricted the energy density of LIBs.[20,21] Among various types of cathode materials, LiFePO$_4$ (LFP) with a theoretical capacity of 170 mAh g^{-1} and an intercalation potential of 3.4 V (vs Li/Li$^+$) has been recognized as one of the representative cathode candidates in LIBs.[22–24] In particular, a stable 3D-olivine framework of LFP provides facile ion diffusion pathways during continued charge/discharge processes, ensuring long-term stability with structural integrity.[25,26] However, the inherently low electrical conductivity of LFP (<10^{-9} S cm^{-1}) requires blending (or mixing) with conductive carbon materials for power performance despite a notable loss of volumetric energy density.[27] Additionally, most LFP materials reported to date have relatively large sizes (hundreds of nm to a few μm) and exhibit extremely low dispersion stability in organic media,[23,28] which is difficult to deeply, uniformly, and densely incorporate into highly porous textiles. Furthermore, the presence of insulating elements (i.e., polymer linker and/or bulky organic ligands) covering the LFP surface also seriously restricts the charge transfer within the electrode. Therefore, efficient incorporation of high-quality LFP nanomaterials with controllable surface ligand structures into porous conductive textiles through a solution-based deposition process is essential for minimizing the charge transfer resistance between each electrode components.

Herein, we introduce a high-performance textile-based LIB cathode with high specific/areal capacities and high rate capability using interfacial assembly approaches (i.e., hydrogen bonding layer-by-layer (LbL) assembly (H-bonding assembly) and ligand replacement reaction-mediated LbL assembly (LRR assembly)). In particular, our approach can directly bridge all the interfaces existing among textiles, conductive components, and/or energy NPs without unnecessary insulating organics (including polymer binders and/or bulky organic ligands) (**Scheme 1**). Furthermore, our approach allows the conformal coating of conductive components onto the surface of homogeneously distributed energy NPs without any agglomerations or segregations of NPs, resulting in enhanced electron transfer at all interfaces within the electrode. For this study, well-defined LFP NPs with a size of ≈35 nm were newly synthesized using dioleamide (DA) stabilizers in nonpolar media. The noticeable features of dioleamide-stabilized LiFePO$_4$ nanoparticles (DA-LFP NPs) are that bulky DA ligands bound to the surface of LFP NPs can be easily removed by amine (NH$_2$)-functionalized multiwalled carbon nanotubes (MWNT-NH$_2$) due to the higher affinity (i.e., covalent bonding) between the bare surface of LFP NPs and the NH$_2$ groups of MWNT-NH$_2$, and additionally, the LFP NPs can be densely yet uniformly deposited onto the surface of MWNT-NH$_2$. Notably, this adsorption behavior cannot be realized by typical approaches (the slurry casting process or electrostatic LbL assembly performed in aqueous media) as well as by conventional large LFP particles (size approximately a few micrometers) with poor dispersion stability in the solvent.

The conductive textiles (current collector) were prepared through a consecutive H-bonding assembly of chemically modified MWNT-NH$_2$ and MWNT-COOH (i.e., MWNT multilayer composite) onto 600 μm thick cellulose textiles in organic media. The formation of robust conductive textiles with large amounts of NH$_2$ groups could easily induce the dense packing of DA-LFP NPs onto the entire area of the textiles by the abovementioned LRR assembly process, and furthermore, the loading mass of the adsorbed DA-LFP NPs could be continuously increased through consecutive LRR assembly between the DA-LFP NPs and MWNT-NH$_2$. In this case, a number of oxygen functional groups on MWNT-COOH not only act as linkers to form stable MWNT networks but also provide additional reversible capacity through redox reactions with Li ions. Importantly, the LbL-assembled textile electrode effectively preserved the mechanical properties of the textiles despite the high loading mass of active nanomaterials (i.e., LFP NPs and MWNTs), enabling a further increase in the areal capacity by a simple folding process without significant performance fading. Based on this unique approach, the full utilization of the porous structure of cellulose textiles delivered remarkably high specific and areal capacities (196 mAh g^{-1} and 8.3 mAh cm^{-2} at 17 mA g^{-1}, respectively). These high-performance indices were superior to those of previously reported LFP-based textile cathodes as well as LiCoO$_2$-based cathodes with a higher theoretical capacity (≈272 mAh g^{-1}) and charge (Li$^+$/electron) conductivity.[29,30] Furthermore, the LRR-assembled textile electrode exhibited superior rate capability by delivering specific and areal capacities of 85.6 mAh g^{-1} at 10 C (15.2 mg cm^{-2}) and ≈5.7 mAh cm^{-2}
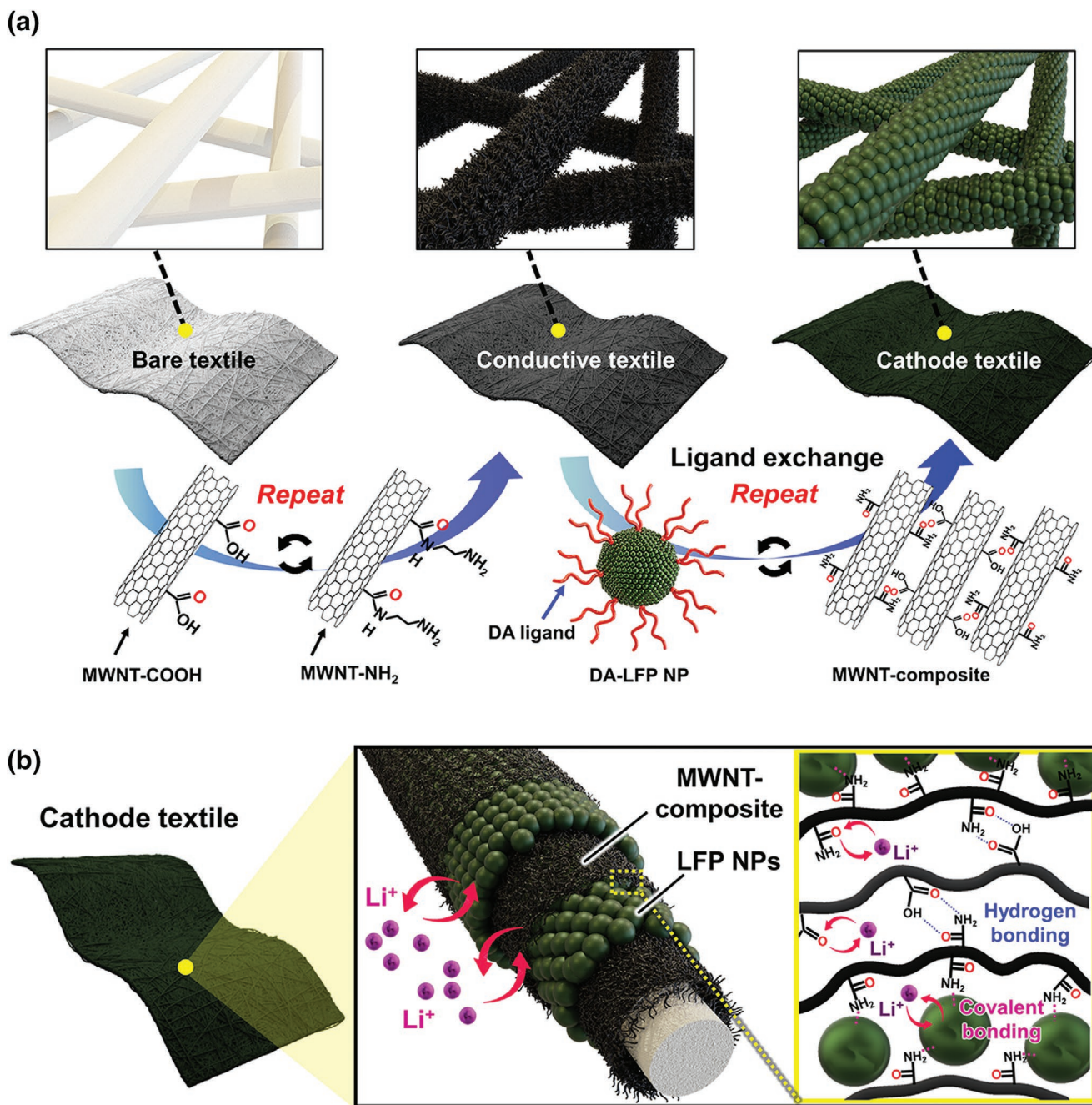
Scheme 1. a) Schematic illustration of the fabrication process of textile-based cathode electrodes through ligand replacement reaction-mediated LbL assembly involving surface ligand modulation of LFP NPs. b) Schematic illustration of the composition and bonding structure of the LRR-assembled active composite layers on the fiber surface. Although the (DA-LFP NP/MWNT-composite)$_m$ multilayers are depicted as the formation of stratified layers for the better understanding of the LRR assembly mediated process, the real structural image is closer to the nanoblended structure due to the random close packing and partially insufficient surface coverage of LFP NPs and/or MWNTs.

at 2 C (45.9 mg cm^{-2}), which was mainly attributed to the significantly reduced resistances. Given that our approach based on the interface design of electrodes can effectively utilize the large surface area of porous textiles and notably improve the charge transfer within textile electrodes, it can provide a basis for developing high-performance textile electrodes for various energy storage devices.

2. Results and Discussion

2.1. LRR Assembly for (DA-LFP NP/MWNT-Composite)$_m$ Multilayers

DA-LFP NPs with a well-ordered olivine structure were successfully synthesized through the solvothermal reaction with

metal precursors and a mixture of oleic acid and oleylamine (dioleamide, DA) (the details are shown in the Experimental Section, Supporting Information). As shown in **Figure 1**a, the high-resolution transmission electron microscopy (HR-TEM) image and the SAED pattern showed that DA-LFP NPs with an average diameter of ≈35 nm had a highly ordered single-crystalline feature with lattice fringe spacings of 0.47 and 1.03 nm assigned to the (001) and (100) crystal planes, respectively.[31,32] The chemical structure and the surface composition of the DA-LFP NPs were also analyzed using X-ray photoelectron spectroscopy (XPS) (Figure S1, Supporting Information). As confirmed by X-ray diffraction patterns, the DA-LFP NPs exhibited an orthorhombic (olivine) crystal structure (*Pnma* space group, JCPDS No. 83–2092)[28] without impurities such as Li_3PO_4. Considering that the presence of impurities in LFP adversely affects the charge storage performance in LIB applications,[33] the DA-LFP NPs synthesized in our study are expected to minimize capacity loss due to structural flaws in nanosized energy storage components (Figure S2, Supporting Information).

Another notable benefit of DA-LFP NPs is that the stable monodentate coordination bonding between the amide group (i.e., −NH) of DA ligands and the surface of LFP[34] provides the excellent colloidal stability in nonpolar solvents as well as the uniform physical structures (i.e., shape and size) of NPs (Figure S3, Supporting Information). Specifically, as shown in the Fourier transform infrared (FTIR) spectroscopy data of Figure 1b, the DA-LFP NP shows the characteristic peaks derived from both DA ligand with long aliphatic chains (i.e., C−H, C=O, and N−H groups found in native DA ligand) and the NP itself (i.e., PO_4^{3-} compound), indicating the formation of the DA ligand onto the LFP NP surface. As a result, the formed DA-LFP NPs exhibited high dispersion stability in toluene without any NP agglomeration and/or precipitation phenomena even after six months, which could have a notable advantage in effectively utilizing the large surface area of the porous textiles during the NP deposition process.

When designing electrodes, insulating organics such as polymeric binders and/or bulky ligands bound to the NP surface inevitably restrict electron transfer at the numerous interfaces existing within the electrode, resulting in increased internal resistance and poor rate capability. To address these critical issues, surface-modified MWNTs (i.e., MWNT-NH₂ and MWNT-COOH) were prepared through a small molecule-based ester coupling reaction,[35] and were used as conductive linkers in the textile electrodes. The well-anchored functional groups (i.e., −NH₂ and −COOH) on the modified MWNT surface were confirmed by FTIR and XPS analysis (Figure S4, Supporting Information). These hydrophilic functional groups of MWNTs can not only provide high dispersion stability in ethanol without any CNT bundles (Figure S5, Supporting Information) but also allow the formation of robust LbL-assembled nanocomposites based on complementary interactions (i.e., hydrogen and covalent bonding) between each electrode component (MWNTs, LFP NPs, and cellulose textile) (Figure S6, Supporting Information). In particular, the high affinity between the NH₂ groups of MWNTs and the LFP NPs induced strong multidentate interactions, which led to the efficient removal of bulky DA ligands (having monodentate coordination with the LFP NP surface) during consecutive LbL assembly (i.e., LRR assembly).[36,37]

Thus, it is inferred that the LbL assembly accompanying the successive interface design of active energy NPs (DA-LFP NPs) can provide better charge transfer kinetics than conventional slurry casting methods that require a certain amount of polymeric binders proportional to the loading amount of the active materials. Additionally, the high electrical conductivity of (MWNT-NH₂/MWNT-COOH/MWNT-NH₂) (MWNT-composite) allows a high rate capability to be maintained even under a high loading of LFP NPs. Moreover, the oxygen-containing groups of MWNT-COOH can also produce additional capacity through redox reactions between oxygen functional groups and Li ions (the details are given in the Section 2.3).

The electrode build-up mechanism based on the in situ surface modification (i.e., LRR) of the LFP NPs was confirmed using FTIR spectroscopy in advanced grazing angle specular reflectance mode during repetitive LRR assembly in organic media (for the (DA-LFP NP/MWNT-composite)$_m$, "m" indicates the periodic number) (Figure 1c; Figure S7, Supporting Information). The first deposition of DA-LFP NPs onto the NH₂-functionalized substrate (i.e., $m = 0.5$) displayed noticeable absorption peaks at 2850, 2950, 1642, and 1544 cm^{-1} originating from C−H, C=O, and N−H bond vibrations of the DA ligands,[38] (see Figure 1b,c). Among these characteristic peaks of the DA-LFP NPs, the C−H stretching bands at 2850 and 2950 cm^{-1} caused by the long aliphatic chains of the DA ligand almost disappeared after the subsequent deposition of the MWNT composite (i.e., $m = 1$) onto the outermost DA-LFP NP layer, suggesting the efficient elimination of bulky DA ligands from the NP surface. In this case, since the vibration bands for the amide groups (i.e., C=O and N−H bonds) and the CH₂ bending of the DA ligand nearly overlap with the peaks originating from the functional groups of MWNT composites (see Figure S4a, Supporting Information), the absorption intensities in this region gradually increased according to the increase in the deposited MWNT layers (see Figure S7, Supporting Information). These phenomena were periodically observed after the sequential deposition of the DA-LFP NP ($m = 1.5$) and MWNT-composite layers ($m = 2$) (Figure 1c), which evidently implied consecutive ligand replacement between the DA ligands and MWNT-NH₂ during LbL deposition.

Another critical challenge in the fabrication of battery electrodes is to ensure that all active components within the electrode are evenly distributed with conductive additives. Particularly, when using nanomaterials such as LFP NPs with poor electrical conductivity, their aggregation adversely affects the electrode capacity under high-rate operation.[39] In this regard, our LRR assembly can provide an important clue for resolving the abovementioned phenomenon.[11,40–43] To confirm this possibility, the growth of the LbL-assembled (DA-LFP NP/MWNT-composite)$_m$ electrode was systematically monitored using UV–vis spectroscopy, a quartz crystal microbalance (QCM) device, and field-emission scanning electron microscopy (FE-SEM) (Figure 1d; Figure S8, Supporting Information). With increasing periodic number (m), the loading mass of the (DA-LFP NP/MWNT-composite)$_m$ multilayers regularly increased with an almost constant composition mass ratio (i.e., 4.9 µg cm⁻² LFP NP per layer and 1.7 µg cm⁻² MWNTs per layer) (Figure 1d). Additionally, the formed (DA-LFP NP/MWNT-composite)$_m$ films exhibited a relatively high mass density of
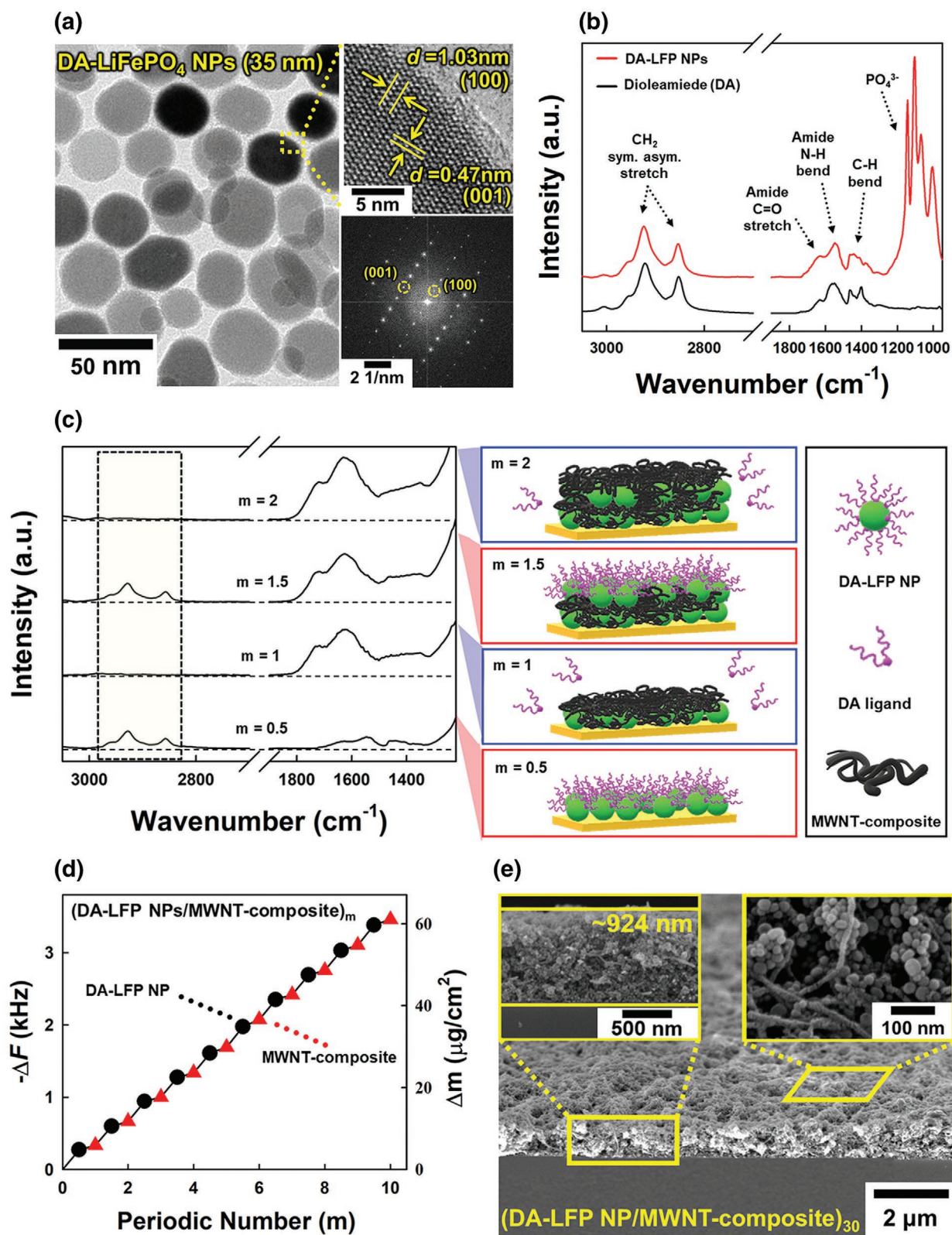
Figure 1. a) HR-TEM images and SAED pattern (bottom right) of as-synthesized DA-LFP NPs. b) FTIR spectra of DA-LFP NPs (top) and raw dioleamide (DA) (bottom). c) FTIR spectra of (DA-LFP NP/MWNT-composite)$_m$ multilayer films as a function of the periodic number (m) (left) and schematic illustration showing multilayer structures during LRR assembly (right). d) QCM analysis of the (DA-LFP NP/MWNT-composite)$_m$ multilayer according to the increase in the periodic number (m). e) Tilted FE-SEM image of (DA-LFP NP/MWNT-composite)$_{30}$ multilayer films. Insets represent cross-section (left) and planar (right) images of the (DA-LFP NP/MWNT-composite)$_{30}$ multilayer films, showing highly porous structures with a number of open pores.

2101631 (5 of 12)

ADVANCED
SCIENCE NEWS
www.advancedsciencenews.com

ADVANCED
ENERGY
MATERIALS
www.advenergymat.de

≈2.0 g cm^{-3} (the density of LiFePO$_4$ is 3.6 g cm^{-3}) despite the use of a low-density MWNT composite (<1 g cm$^{-3[44]}$). It should be noted that the porous structure of the MWNT network was sufficiently maintained due to the formation of densely but uniformly deposited LFP NP arrays onto the MWNT fibers without NP aggregations (Figure 1e).

2.2. Preparation of (DA-LFP NP/MWNT-Composite)$_m$-Coated Conductive Textiles

Next, using commercially available cellulose textiles, we prepared the (DA-LFP NP/MWNT-composite)$_m$-based flexible LIB cathode. MWNT-NH$_2$ and MWNT-COOH were first LbL-assembled onto the textiles via hydrogen bonding interactions, converting insulating textiles to electrically conductive textiles. As the bilayer number (n) of the (MWNT-COOH/MWNT-NH$_2$)$_n$ multilayer increased from 1 to 20, the sheet resistance gradually decreased from 2.3 × 10^5 to 3.6 × 10^3 Ω sq^{-1} (Figure S9, Supporting Information). In this case, the MWNT nanocomposites on the textile produced a large amount of nanopores as well as macropores. As a result, the (MWNT-COOH/MWNT-NH$_2$)$_{20}$-coated textile electrodes exhibited an ≈2 times higher specific surface area (≈0.702 m^2 g^{-1}) than that of the bare textile (≈0.384 m^2 g^{-1}) (Figure S10, Supporting Information), which allows a larger amount of LFP NP loading within the electrode. Then, the DA-LFP NP was alternately deposited onto the abovementioned conductive textile (i.e., (MWNT-COOH/MWNT-NH$_2$)$_{20}$-coated textile) with the MWNT composite via LRR assembly. During this assembly process, the well-dispersed DA-LFP NPs in toluene could be effectively incorporated into all the accessible surface areas of the textile electrode, resulting in the formation of uniformly distributed NP arrays within the electrode without any significant NP agglomeration, as confirmed by FE-SEM and energy-dispersion spectroscopy (EDS) mapping images (**Figure 2**a). Specifically, the surface morphology of the (DA-LFP/MWNT-composite)$_{30}$-coated textile was almost similar to that of bare textile (Figure 2b), indicating efficient utilization of the textile surface through accurate control of the film growth. As a result, the loading amount of active materials on the textile-based electrode was ≈83 times higher than that on a nonporous flat substrate (i.e., the QCM substrate) (Figure 2c). Our approach can also be easily applied to large-area textiles (Figure S11, Supporting Information).

In addition to these advantages, the most notable feature of our approach lies in the fact that well-defined, high-quality energy nanomaterials can be effectively incorporated into porous textile substrates through strong interfacial interactions. Notably, the conventional slurry casting method cannot induce the formation of a homogeneously distributed active material network within the porous textiles due to the high viscosity of the slurry and the unfavorable interaction between current collector and active components as well as between neighboring active components (Figure S12, Supporting Information). As mentioned earlier, the aggregation of energy materials with poor conductivity can severely limit ion diffusion and charge transfer within the electrode, resulting in a significant loss of energy efficiency and rate capability. Another benefit of our approach is that the (DA-LFP NP/MWNT-composite)$_{30}$-coated

textile electrode could exhibit excellent mechanical/electrical stability. Specifically, our textile electrodes could preserve almost 100% of the initial electrical conductivity even after 5000 bending cycles (Figure 2d). By contrast, the slurry-cast textile electrode showed serious mechanical/electrical damage (i.e., cracks and delamination) (Figure S13, Supporting Information). These results clearly suggest that our approach is beneficial for taking advantage of the textile's structural characteristics (i.e., large available surface area and flexibility) and for strengthening interfacial robustness when fabricating textile-based energy electrodes.

2.3. Electrochemical Properties of (DA-LFP NP/MWNT-Composite)$_m$-Coated Conductive Textiles for LIB Cathodes

We investigated the electrochemical behavior of (DA-LFP NP/MWNT-composite)$_m$-coated textile electrodes (textile cathodes) using galvanostatic charge/discharge (GCD) measurements, cyclic voltammetry (CV), and electrochemical impedance spectroscopy. As shown in **Figure 3**a, the GCD profiles of the textile cathodes at a current density of 17 mA g^{-1} (i.e., 0.1 C) in the potential range of 1.8–4.2 V (vs Li/Li$^+$) exhibited typical voltage plateaus at ≈3.4 V, originating from the phase transition of the LFP NPs during Li-ion insertion/extraction processes (i.e., the Li$_x$FePO$_4$ phase according to the x value ranging from 0 to 1).[25,45] In this case, the areal capacities of these cathodes increased from 1.1 to 2.9 mAh cm^{-2} with increasing periodic number (m) (i.e., loading amount of active materials) from 10 to 30 (corresponding areal mass densities were 5.5 for m = 10, 10.2 for m = 20, and 15.2 mg cm^{-2} for m = 30) (Figure 3b). Despite an increase in the total loading mass of DA-LFP NPs by sequential LbL deposition, the specific capacity of the cathodes showed negligible changes (i.e., from 196 (m = 10) to 191 mAh g^{-1} (m = 30)). These results indicate the uniform coating of the porous and conducting active composite networks (i.e., LFP NP/MWNT-composite multilayers) on the surface of textile fibers without any agglomeration and/or segregation, as already shown in Figure 2a–c. In this case, the gravimetric and volumetric energy density were calculated to be ≈152 Wh L^{-1} and ≈607 Wh kg^{-1}, respectively, based on the total volume and mass of the textile cathode electrode. When the periodic number (m) was further increased up to 60 (the areal mass density: 30.8 mg cm^{-2}), the areal capacities of the (DA-LFP NP/MWNT-composite)$_m$-based textile electrodes were significantly enhanced up to 5.7 mAh g^{-1} (at 17 mA g^{-1}). The corresponding specific capacity (i.e., 185 mAh g^{-1} for m = 10) was 94.3% of the specific capacity for m = 10 (Figure S14, Supporting Information). These results evidently suggest that our approach is very useful for achieving high areal capacity without compromising the specific capacity of active materials (Figure S15, Supporting Information).

We also investigated the possibility that MWNT composites can contribute to the improvement in the overall capacities of textile cathodes. It has been reported that oxygen-containing functional groups (including carbonyl groups) grafted onto the surface of carbon-based materials (i.e., MWNTs and graphene) can induce a reversible Faradaic reaction with Li ions (e.g., C = O + Li$^+$ ↔ C–O–Li), delivering a high specific capacity.[46–49]
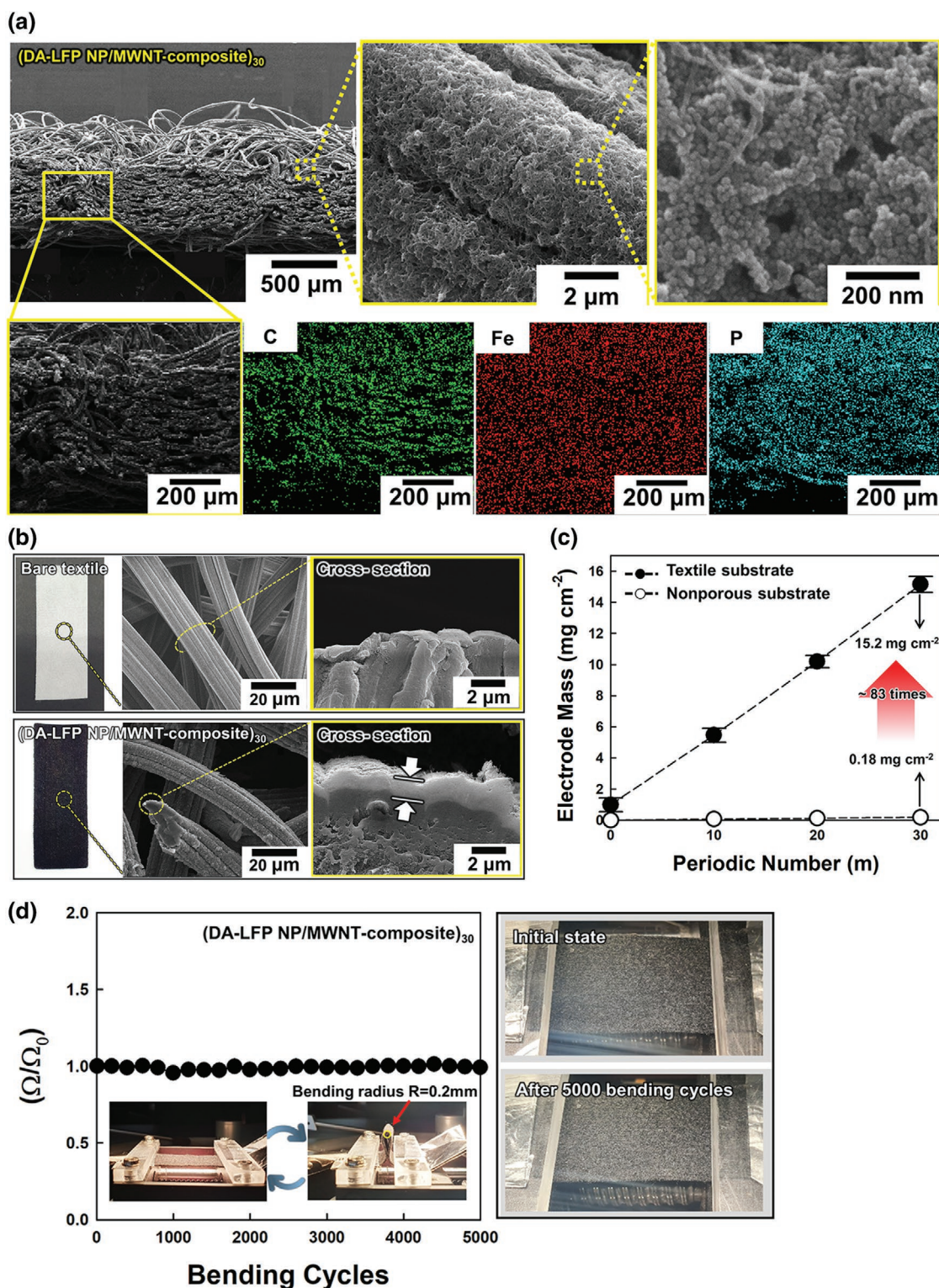
Figure 2. a) Cross-sectional and high-magnification FE-SEM images of (DA-LFP NP/MWNT-composite)$_{30}$-coated textile electrodes (top) and the corresponding EDS elemental mapping images for C, Fe, and P (bottom). b) Digital images and the corresponding FE-SEM images of bare textile (top) and (DA-LFP NP/MWNT-composite)$_{30}$-coated textile electrodes (bottom). Cross-sectional FE-SEM images (yellow solid box) of each sample show well-coated (DA-LFP NP/MWNT-composite)$_{30}$ films on the textile fiber. c) Comparison of the periodic number (m)-dependent electrode mass change between textile- and nonporous flat substrate (i.e., gold-coated QCM electrode)-based electrodes. d) Electrical stability of (DA-LFP NP/MWNT-composite)$_{30}$-coated textile electrodes under repetitive bending cycle tests (300 times) with a bending radius of 0.2 mm. Insets indicate digital images of textile electrodes in flat and fully bent states. As a result, the LRR-assembled textile electrodes showed no noticeable mechanical failures even after 5000 bending cycles.
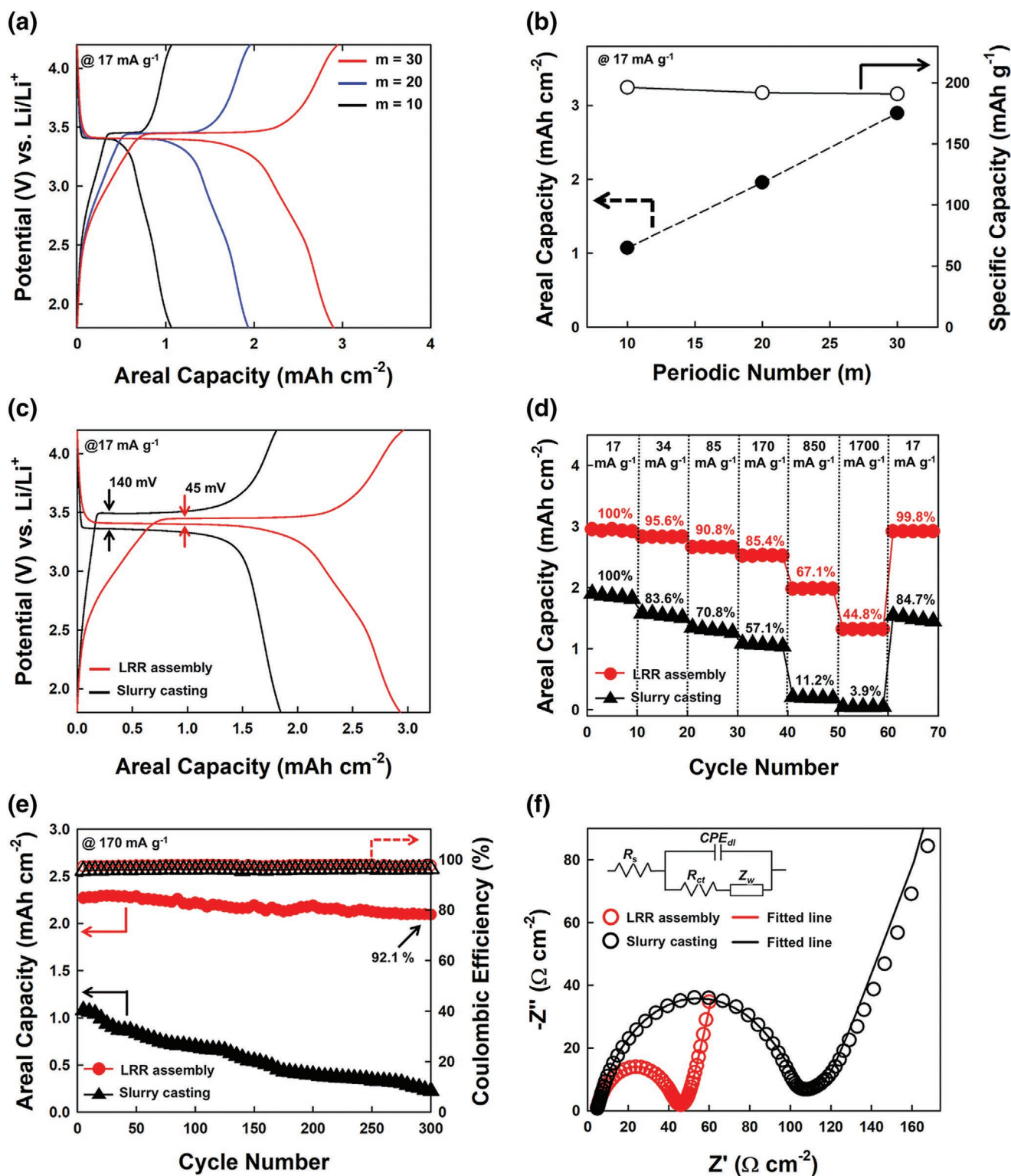
Figure 3. a) Galvanostatic charge/discharge (GCD) profiles of (DA-LFP NP/MWNT-composite)$_m$-coated textile electrodes with different periodic numbers (m = 10, 20, and 30) at a current density of 17 mA g^{-1}. b) Areal and specific capacities of (DA-LFP NP/MWNT-composite)$_m$-coated textile electrodes with increasing periodic number (m). c) GCD profiles (at 17 mA g^{-1}) of textile electrodes prepared by LRR assembly and slurry casting. d) Rate capability of each textile electrode at various current densities from 17 mA g^{-1} to 1.7 A g^{-1}. e) Trances of the areal capacity and coulombic efficiency of each textile electrode as a function of GCD cycles at 170 mA g^{-1}. f) Nyquist plots and the simplified equivalent circuit (inset) of LRR assembly and slurry casting-based textile electrodes.

**ADVANCED
SCIENCE NEWS**
www.advancedsciencenews.com

**ADVANCED
ENERGY
MATERIALS**
www.advenergymat.de

As already confirmed in Figure S4 of the Supporting Information, the MWNT composite (i.e., MWNT-COOH/MWNT-HN$_2$ multilayers) used for the textile cathode contains a number of oxygen functional groups that can undergo reversible redox reactions with Li ions (Figure S16, Supporting Information).[50,51] As shown in Figure S16 of the Supporting Information, the additional redox peaks (near 3.0 V) in the CV scans of the (DA-LFP NP/MWNT-composite)$_{30}$-textile cathode were observed near the characteristic peaks of LFP NPs, which was attributed to the surface redox reactions of the oxygen functional groups in the MWNT composite (Figure S16a, Supporting Information). In this case, the MWNT composite showed high specific and areal capacities of approximately 244 mAh g^{-1} and ≈1.1 mAh cm^{-2}, respectively (Figure S16b, Supporting Information). In particular, this specific capacity value was slightly higher than that of the electrostatic LbL-assembled MWNT composite (≈200 mAh g^{-1}) prepared in water.[46] As a result, the specific capacity of the MWNT composite used in our study gave additional Li storage performance to the (DA-LFP NP/MWNT-composite)$_m$-textile cathodes, thereby allowing a higher specific capacity of 196 mAh g^{-1} (m = 10 at 0.1 C) than the theoretical value (≈170 mAh g^{-1}) of bulk LFP.[49,52]

The superior electrochemical performance of the LRR-assembled (DA-LFP NP/MWNT-composite)$_{30}$-textile cathode could be more clearly revealed through the comparison with that of the conventional textile cathode composed of LFP and MWNTs (i.e., the slurry casting-based textile cathode) (see the Experimental Section, Supporting Information). As shown in Figure 3c, the areal capacity of the slurry-based textile cathode with a relatively high areal mass density of 23.3 mg cm^{-2} was measured to be ≈1.8 mAh cm^{-2}, which was much lower than that (2.9 mAh cm^{-2}) of the LRR-assembled (DA-LFP NP/MWNT-composite)$_{10}$-textile cathode with an areal mass density of 15.2 mg cm^{-2} (for m = 10). Additionally, the slurry-cast textile cathode showed a significantly low specific capacity of ≈79.1 mAh g^{-1}, which corresponded to only 41.4% of the LRR-assembled textile cathode (191 mAh g^{-1} for m = 30) (Figure S17, Supporting Information). Furthermore, the LRR-assembled cathode exhibited a lower electrochemical overpotential (≈45 mV) than the slurry-cast-based electrode (≈140 mV).

To assess the rate capability, the current density-dependent GCD tests for LRR-assembled and slurry casting-based electrodes were compared at various current densities (Figure 3d; Figure S18, Supporting Information). First, the output areal and specific capacities of the two different electrodes gradually decreased with increasing applied current density from 17 to 850 mA g^{-1} (Figure S18, Supporting Information), which was mainly due to insufficient ion diffusion kinetics in fully utilizing the entire surface area of the electrode. However, the LRR assembly-based cathode delivered a much more improved rate capability than the slurry-cast cathode, implying the superior ion accessibility of the LRR-assembled textile cathode. The corresponding rate capabilities of each electrode are shown in Figure 3d. The LRR-assembled textile cathode maintained 44.8% (i.e., 1.3 mAh cm^{-2}) of the initial areal capacity (i.e., 2.9 mAh cm^{-2} at 17 mA g^{-1}) at 1700 mA g^{-1} (or 10 C). By contrast, the slurry-cast textile electrodes delivered only 3.9% (0.05 mAh cm^{-2}) of the initial capacity value at 1700 mA g^{-1}. In addition, the capacity retention and the corresponding

coulombic efficiency of each electrode were evaluated under continuous GCD cycling at a current density of 170 mA g^{-1} (Figure 3e). In this case, the LRR-assembled textile electrodes delivered 92.1% (≈2.1 mAh cm^{-2}) of their initial areal capacity value with a high coulombic efficiency of 96.5% even after 300 cycles, while the slurry-cast electrode showed only 20.8% (0.2 mAh cm^{-2}) with a relatively lower coulombic efficiency of 95.2%. This superior electrochemical stability of the LRR-assembled textile electrodes is attributed to the stable connection of all electrode components within the electrode by strong interfacial interactions.

Additionally, the Nyquist plots show that the LRR-assembled electrodes exhibited considerably lower R_{ct} values (39.3 Ω cm^{-2}) than the slurry-cast electrodes (98.4 Ω cm^{-2}), indicating much improved charge transfer kinetics at the electrode/electrolyte interfaces. That is, the homogeneous distribution of LFP NPs within the MWNT networks through LRR assembly allows fast and facile access of charge carriers to the LFP NP surfaces (Figure 3f). As a result, this efficient electrode structure generated a high rate capability and cycle retention (Figures S19 and S20, Supporting Information).

2.4. Preparation of Foldable (DA-LFP NP/MWNT-Composite)$_m$-Coated Conductive Textiles

Folding textile electrodes can be a simple and effective way to dramatically increase the energy density per unit area.[53,54] Therefore, we also investigated the electrochemical performance of LRR-assembled textile electrodes (i.e., (DA-LFP NP/WMNT-composite)$_{30}$-coated textile) in the multifold states (**Figure 4**). Here, since folding was performed in a zigzag pattern with an electrode area of 1 × 1 cm^2 (Figure 4a), the areal mass density of the electrodes increased in proportion to the folding number. As shown in Figure 4b, the LRR-assembled textile electrodes did not show any serious cracks or delamination of active materials on the bent edge even in the fully folded state, indicating superior mechanical stability compared to the slurry-cast textile electrodes, which showed severe structural damage after folding (Figure S21, Supporting Information). Therefore, we first performed the folding number-dependent GCD measurements of the LRR-assembled textile electrodes (i.e., (DA-LFP NP/MWNT-composite)$_{30}$-coated textile) at 17 mA g^{-1} (Figure 4c; Figure S22, Supporting Information). In this case, the LRR-assembled textile electrode delivered areal capacities of 2.9, 5.6, and 8.3 mAh cm^{-2} at folding numbers of 0 (unfolded), 1, and 2, respectively, which are almost proportional to the increase in the areal mass density of the electrodes (i.e., 15.2, 30.5, and 45.9 mg cm^{-2} for 0, 1, and 2 folds, respectively). Additionally, the specific capacity of the LRR-assembled textile electrodes was maintained at 180.2 mAh g^{-1} at a twofold state (areal mass density: 45.9 mg cm^{-2}), which corresponded to 94.3% of the unfolded electrodes (191.1 mAh g^{-1}). These stable performance outputs under a gradual increase in areal mass density imply that the well-connected porous structure of the textile electrode is stably maintained even after multiple folding cycles. For example, although the 1-folded textile electrodes showed a similar areal capacity to that of the (DA-LFP NP/WMNT-composite)$_{60}$-coated textile electrodes due to almost

ADVANCED
SCIENCE NEWS
www.advancedsciencenews.com

ADVANCED
ENERGY
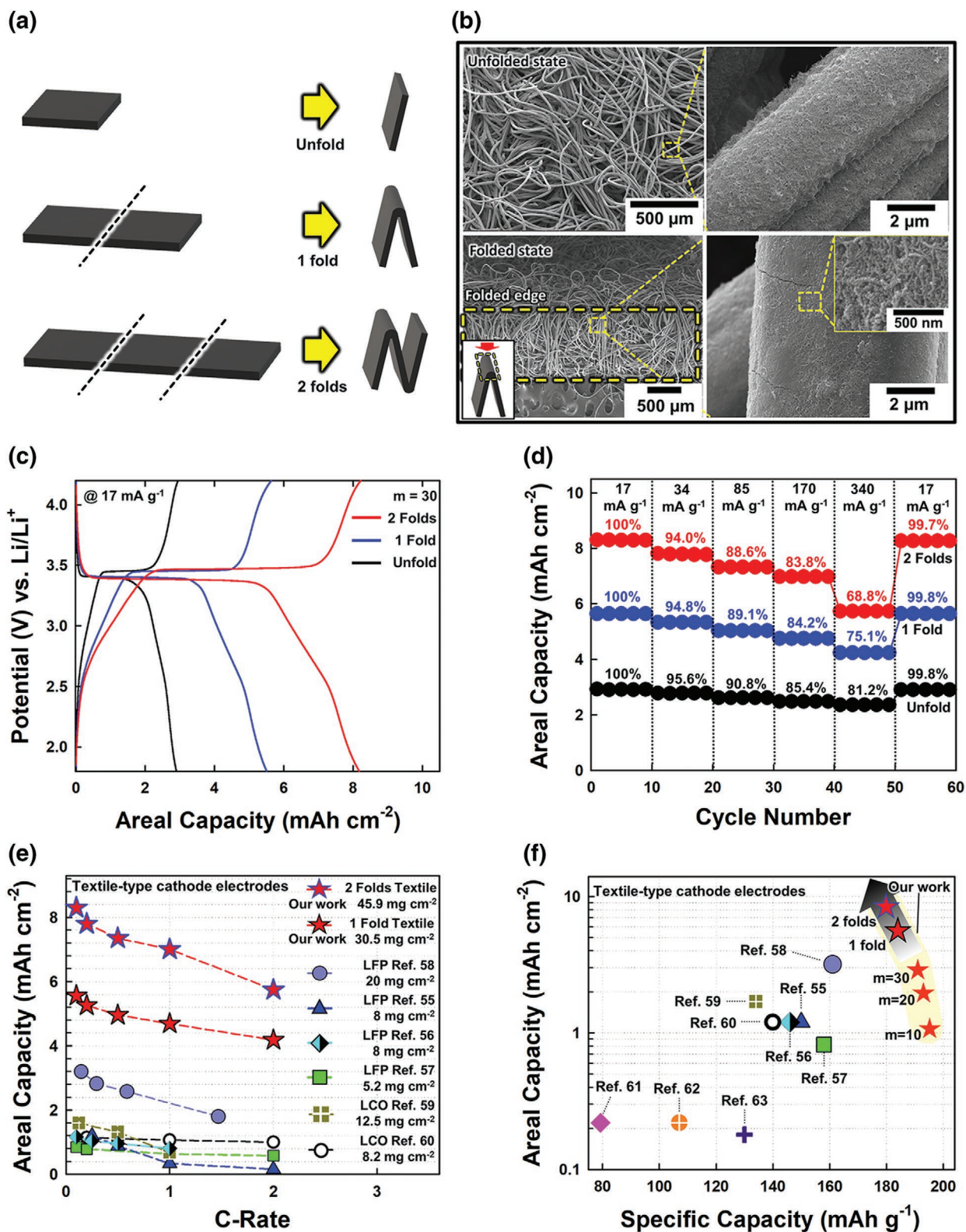**MATERIALS**
www.advenergymat.de

Figure 4. a) Schematic illustration showing the zigzag folding approach for the textile electrodes. b) FE-SEM images of the LRR-assembled textile electrodes in the initial (unfold, top) and folded states (bottom). Folding number-dependent **c)** GCD profiles and d) rate capability of (DA-LFP NP/MWNT-composite)$_{30}$-coated textile electrodes measured at various current densities. e) Comparison of the current density-dependent areal capacity of twofold LRR-assembled textile electrodes with previously reported textile-based cathode electrodes. f) Comparison of the areal and specific capacities of our results with previously reported textile-type cathode electrodes prepared using 3D-porous host materials.

the same areal mass density, the overpotential between charge/discharge plateaus (redox potential) is much lower (≈49 mV) than that of the unfolded textile electrodes (≈180 mV) with a thicker film thickness (i.e., active layer) (see Figure S14, Supporting Information), indicating lower internal resistance.

The rate performance of each folded textile electrode was investigated through sequential GCD cycling at various current densities ranging from 17 to 340 mAh g^{-1} (Figure 4d). The areal capacity of the folded electrodes gradually decreased as the applied current density increased, and these trends became more pronounced as the folding number increased due to the increased electrode thickness. The high areal capacities of the folded textile electrodes recorded at 340 mA g^{-1} (2 C) (4.2 and 5.7 mAh cm^{-2} for one- and twofolded states) greatly exceeded those of the reported textile-type cathode electrodes fabricated by single-layer slurry casting or filtration methods of LFP or LCO particles (Figure 4e).[55–60] The fitted Nyquist plots showed that as the number of folds (i.e., areal mass density) of the textile electrodes increased to 1 and 2, the R_{ct} values increased to 86.9 and 128.5 Ω cm^{-2}, respectively (Figure S23, Supporting Information). On the other hand, the Warburg impedance coefficients of the folded electrodes were measured to be ≈1.5 Ω s$^{-0.5}$, similar to that of the unfolded electrode (Figure S24, Supporting Information). These results suggest that although the R_{ct} values increase with folding due to the increased loading of the active material, the well-preserved internal porous structure and conducting networks allow efficient charge transfer within the electrodes. As a result, the LbL-assembled textile electrodes (i.e., (DA-LFP NP/WMNT-composite)$_m$-coated textiles) delivered high specific and areal capacities of 191 mAh g^{-1} (maximum value is 196 mAh g^{-1} at m = 10) and 8.3 mAh cm^{-2} for unfolded and 2-folded (DA-LFP NP/MWNT-composite)$_{30}$ textile electrodes, respectively. Thus, it is worth noting that our approach can simultaneously increase the areal and specific capacities by minimizing the internal resistance caused by mass loading of active materials through LbL assembly based on controlled interface design (ligand exchange reaction), resulting in superior electrochemical performance compared to the reported LFP- or LCO-based textile-type electrodes (Figure 4f).[55–63]

3. Conclusion

We have demonstrated that textile-based LIB cathodes with high areal capacity, excellent rate capability, and long-term cycle retention can be realized through interfacial LRR assembly of high-quality energy nanomaterials (i.e., LFP NPs and MWNTs). The highlight of our approach is that the well-defined, strong interactions between all electrode components (i.e., active materials and textile substrate) allow the formation of dense and uniformly distributed active composite films (i.e., (DA-LFP NP/MWNT-composite)$_m$ multilayers) on all accessible surfaces of the textile substrate without any noticeable agglomerations, thereby preserving the textile's physical nature (i.e., porous structure with excellent mechanical flexibility) even after high loading of active materials. In particular, covalent bonding between LFP NPs and MWNT-NH$_2$ (specifically, amine groups on the MWNT surface) induces efficient elimination of insulating organic ligands (i.e., DA) on the LFP NP surface,

significantly lowering the internal resistance (particularly, originating from contact resistance at interfaces) of the electrodes. These promising features of the LRR-assembled textile electrodes enabled a high areal capacity of 2.9 mAh cm^{-2} (i.e., 191 mAh g^{-1} for areal mass density of 15.2 mg cm^{-2}) at 17 mA g^{-1} (0.1 C) with high rate capability, which far exceeded the performance of conventional slurry-cast electrodes. Importantly, the excellent structural stability of the LRR-assembled textile electrodes allowed us to further increase the areal capacity up to 8.3 mAh cm^{-2} (for 45.9 mg cm^{-2} at 17 mA g^{-1}) by simple folding without significant loss of specific capacity and rate capability. Thus, these results demonstrate that our approach based on the interfacial chemistry of nanomaterials can be applied to various types of electrochemical energy storage systems using substrates with a high specific surface area-to-volume ratio (e.g., textiles) to achieve higher areal performance than conventional slurry casting methods. The introduced LRR electrode assembly process provides a powerful strategy for overcoming charge transport limitations in designing next-generation electrochemical energy devices.

Conflict of Interest

The authors declare no conflict of interest.

Data Availability Statement

Research data are not shared.

[1] J.-M. Kim, C.-H. Park, Q. Wu, S.-Y. Lee, *Adv. Energy Mater.* **2016**, *6*, 1501594.
[2] Y. Zhu, M. Yang, Q. Huang, D. Wang, R. Yu, J. Wang, Z. Zheng, D. Wang, *Adv. Mater.* **2020**, *32*, 1906205.

[3] U. Gulzar, S. Goriparti, E. Miele, T. Li, G. Maidecchi, A. Toma, F. D. Angelis, C. Capiglia, R. P. Zaccaria, *J. Mater. Chem. A* **2016**, *4*, 16771.

[4] S.-H. Park, P. J. King, R. Tian, C. S. Boland, J. Coelho, C. J. Zhang, P. McBean, N. McEvoy, M. P. Kremer, D. Daly, J. N. Coleman, V. Nicolosi, *Nat. Energy* **2019**, *4*, 560.

[5] Y. Kuang, C. Chen, D. Kirsch, L. Hu, *Adv. Energy Mater.* **2019**, *9*, 1901457.

[6] J. Chang, Q. Huang, Z. Zheng, *Joule* **2020**, *4*, 1346.

[7] J. Chang, Q. Huang, Y. Gao, Z. Zheng, *Adv. Mater.* **2021**, 2004419, https://doi.org/10.1002/adma.202004419.

[8] R. Lu, M. Cheng, L. Mao, M. Zhang, H. Yuan, K. Amin, C. Yang, Y. Cheng, Y. Meng, Z. Wei, *EcoMat* **2020**, *2*, 12010.

[9] Z. Wang, X. Li, Z. Yang, H. Guo, Y. J. Tan, G. J. Susanto, W. Cheng, W. Yang, B. C. K. Tee, *EcoMat* **2021**, *3*, 12073.

[10] Q. Huang, D. Wang, Z. Zheng, *Adv. Energy Mater.* **2016**, *6*, 1600783.

[11] Y. Ko, M. Kwon, W. K. Bae, B. Lee, S. W. Lee, J. Cho, *Nat. Commun.* **2017**, *8*, 536.

[12] D. Chen, Z. Lou, K. Jiang, G. Shen, *Adv. Funct. Mater.* **2018**, *28*, 1805596.

[13] Y. Gao, C. Xie, Z. Zheng, *Adv. Energy Mater.* **2021**, *11*, 2002838.

[14] H. Sun, S. Xie, Y. Li, Y. Jiang, X. Sun, B. Wang, H. Peng, *Adv. Mater.* **2016**, *28*, 8431.

[15] L. Hu, W. Chen, X. Xie, N. Liu, Y. Yang, H. Wu, Y. Yao, M. Pasta, H. N. Alshareef, Y. Cui, *ACS Nano* **2011**, *5*, 8904.

[16] K. Jost, D. Stenger, C. R. Perez, J. K. McDonough, K. Lian, Y. Gogotsi, G. Dion, *Energy Environ. Sci.* **2013**, *6*, 2698.

[17] L. Bao, X. Li, *Adv. Mater.* **2012**, *24*, 3246.

[18] L. Allison, S. Hoxie, T. L. Andrew, *Chem. Commun.* **2017**, *53*, 7182.

[19] L. Hu, F. L. Mantia, H. Wu, X. Xie, J. McDonough, M. Pasta, Y. Cui, *Adv. Energy Mater.* **2011**, *1*, 1012.

[20] M. Winter, J. O. Besenhard, M. E. Spahr, P. Novák, *Adv. Mater.* **1998**, *10*, 725.

[21] C. Liu, Z. G. Neale, G. Cao, *Mater. Today* **2016**, *19*, 109.

[22] S.-Y. Chung, J. T. Bloking, Y.-M. Chiang, *Nat. Mater.* **2002**, *1*, 123.

[23] L.-X. Yuan, Z.-H. Wang, W.-X. Zhang, X.-L. Hu, J.-T. Chen, Y.-H. Huang, J. B. Goodenough, *Energy Environ. Sci.* **2011**, *4*, 269.

[24] M. S. Islam, C. A. J. Fisher, *Chem. Soc. Rev.* **2014**, *43*, 185.

[25] A. K. Padhi, K. S. Nanjundaswamy, J. B. Goodenough, *J. Electrochem. Soc.* **1997**, *144*, 1188.

[26] A. Manthiram, *Nat. Commun.* **2020**, *11*, 1550.

[27] N. Nitta, F. Wu, J. T. Lee, G. Yushin, *Mater. Today* **2015**, *18*, 252.

[28] J. Jiang, W. Liu, J. Chen, Y. Hou, *ACS Appl. Mater. Interfaces* **2012**, *4*, 3062.

[29] M. Okubo, E. Hosono, J. Kim, M. Enomoto, N. Kojima, T. Kudo, H. Zhou, I. Honma, *J. Am. Chem. Soc.* **2007**, *129*, 7444.

[30] L. Xue, S. V. Savilov, V. V. Lunin, H. Xia, *Adv. Funct. Mater.* **2018**, *28*, 1705836.

[31] Y. Zhao, L. Peng, B. Liu, G. Yu, *Nano Lett.* **2014**, *14*, 2849.

[32] J. Song, B. Sun, H. Liu, Z. Ma, Z. Chen, G. Shao, G. Wang, *ACS Appl. Mater. Interfaces* **2016**, *8*, 15225.

[33] D. Y. W. Yu, K. Donoue, T. Kadohata, T. Murata, S. Matsuta, S. Fujitani, *J. Electrochem. Soc.* **2008**, *155*, A526.

[34] C. Cara, A. Musinu, V. Mameli, A. Ardu, D. Niznansky, J. Bursik, M. A. Scorciapino, G. Manzo, C. Cannas, *Cryst. Growth Des.* **2015**, *15*, 2364.

[35] H. Bao, Y. Pan, Y. Ping, N. G. Sahoo, T. Wu, L. Li, J. Li, L. H. Gan, *Small* **2011**, *7*, 1569.

[36] H. Mattoussi, J. M. Mauro, E. R. Goldman, G. P. Anderson, V. C. Sundar, F. V. Mikulec, M. G. Bawendi, *J. Am. Chem. Soc.* **2000**, *122*, 12142.

[37] J. Yun, Y. Song, I. Cho, Y. Ko, C. H. Kwon, J. Cho, *Nanoscale* **2019**, *11*, 17815.

[38] M. B. Mohamed, K. M. AbouZeid, V. Abdelsayed, A. A. Aliarash, M. S. El-Shall, *ACS Nano* **2010**, *4*, 2766.

[39] X. Lu, A. Bertei, D. P. Finegan, C. Tan, S. R. Daemi, J. S. Weaving, K. B. O'Regan, T. M. M. Heenan, G. Hinds, E. Kendrick, D. J. L. Brett, P. R. Shearing, *Nat. Commun.* **2020**, *11*, 2079.

[40] M. N. Hyder, S. W. Lee, F. C. Cebeci, D. J. Schmidt, Y. Shao-Horn, P. T. Hammond, *ACS Nano* **2011**, *5*, 8552.

[41] D. Nam, Y. Heo, S. Cheong, Y. Ko, J. Cho, *Appl. Surf. Sci.* **2018**, *440*, 730.

[42] Y. Ko, M. Kwon, Y. Song, S. W. Lee, J. Cho, *Adv. Funct. Mater.* **2018**, *28*, 1804926.

[43] Y. Ko, C. H. Kwon, S. W. Lee, J. Cho, *Adv. Mater.* **2020**, *32*, 2001924.

[44] S. W. Lee, B.-S. Kim, S. Chen, Y. Shao-Horn, P. T. Hammond, *J. Am. Chem. Soc.* **2009**, *131*, 671.

[45] D. Li, H. Zhou, *Mater. Today* **2014**, *17*, 451.

[46] S. W. Lee, N. Yabuuchi, B. M. Gallant, S. Chen, B.-S. Kim, P. T. Hammond, Y. Shao-Horn, *Nat. Nanotechnol.* **2010**, *5*, 531.

[47] S. W. Lee, B. M. Gallant, Y. Lee, N. Yoshida, D. Y. Kim, Y. Yamada, S. Noda, A. Yamada, Y. Shao-Horn, *Energy Environ. Sci.* **2012**, *5*, 5437.

[48] T. Liu, K. C. Kim, R. Kavian, S. S. Jang, S. W. Lee, *Chem. Mater.* **2015**, *27*, 3291.

[49] L.-H. Hu, F.-Y. Wu, C.-T. Lin, A. N. Khlobystov, L.-J. Li, *Nat. Commun.* **2013**, *4*, 1687.

[50] L. Kavan, R. Bacsa, M. Tunckol, P. Serp, S. M. Zakeeruddin, F. L. Formal, M. Zukalova, M. Graetzel, *J. Power Sources* **2010**, *195*, 5360.

[51] S. W. Lee, B. M. Gallant, H. R. Byon, P. T. Hammond, Y. Shao-Horn, *Energy Environ. Sci.* **2011**, *4*, 1972.

[52] Q. Zhao, Y. Zhang, Y. Meng, Y. Wang, J. Ou, Y. Guo, D. Xiao, *Nano Energy* **2017**, *34*, 408.

[53] Q. Cheng, Z. Song, T. Ma, B. B. Smith, R. Tang, H. Yu, H. Jiang, C. K. Chan, *Nano Lett.* **2013**, *13*, 4969.

[54] Z. Lv, W. Li, L. Yang, X. J. Loh, X. Chen, *ACS Energy Lett.* **2019**, *4*, 606.

[55] S. H. Ha, K. H. Shin, H. W. Park, Y. J. Lee, *Small* **2018**, *14*, 1703418.

[56] S. Leijonmarck, A. Cornell, G. Lindbergh, L. Wagberg, *J. Mater. Chem. A* **2013**, *1*, 4671.

[57] G. Tian, F. Scheiba, L. Pfaffmann, A. Fiedler, V. S. K. Chakravadhanula, G. Balachandran, Z. Zhao, H. Ehrenberg, *Electrochim. Acta* **2018**, *283*, 1375.

[58] Y. Kuang, C. Chen, G. Pastel, Y. Li, J. Song, R. Mi, W. Kong, B. Liu, Y. Jiang, K. Yang, L. Hu, *Adv. Energy Mater.* **2018**, *8*, 1802398.

[59] A. M. Gaikwad, B. V. Khau, G. Davies, B. Hertzberg, D. A. Steingart, A. C. Arias, *Adv. Energy Mater.* **2015**, *5*, 1401389.

[60] J. H. Han, K. H. Shin, Y. J. Lee, *ACS Appl. Mater. Interfaces* **2021**, *13*, 6375.

[61] K. Kretschmer, B. Sun, X. Xie, S. Chen, G. Wang, *Green Chem.* **2016**, *18*, 2691.

[62] M.-S. Balogun, W. Qiu, F. Lyu, Y. Luo, H. Meng, J. Li, W. Mai, L. Mai, Y. Tong, *Nano Energy* **2016**, *26*, 446.

[63] Q. Xia, M. Ni, M. Chen, H. Xia, *J. Mater. Chem. A* **2019**, *7*, 6187.